Central European Journal of Energetic Materials
ISSN 1733-7178; e-ISSN 2353-1843

Cent. Eur. J. Energ. Mater. 2017, *14*(3): 688-707; DOI: 10.22211/cejem/76335

Study on the State of Internal Stress and Strain of TATB-based Polymer Bonded Explosive Using Strain Markers and Cone-Beam Computed Tomography

Bin Dai, Lin-gang Lan, Wei-bin Zhang, Yong Tian*

Institute of Chemical Materials, CAEP,
64 Mianshan road, 621900 Mianyang, China
**E-mail: icmcaep@163.com*

Abstract: Precise measurement of the inner structural strain of polymer bonded explosive (PBXs) granules during compression molding is highly desirable in order to investigate the inner stress distribution field and its underlying generation mechanism, with the aim of improving the stress distribution uniformity. In this contribution, TATB-based (1,3,5-triamino-2,4,6-trinitrobenzene) PBX granules were formulated and the stress-strain state of the PBX granules during the warm molding process was analyzed. Strain markers were implanted at different locations and the deformation characteristics and regularity of the embedded spherical strain markers were obtained by X-ray micro-tomography. Thus the local strain states at different locations could be obtained, and the local stress state could be deduced. The results showed that axisymmetric deformation occurred in all of the strain markers, where the flat strain ellipsoids were mainly compressed uni-axially. In the central region, the stress was mainly in an axial direction, and the shear force was small. Not only axial stresses, but also large shear stresses in the surrounding region of the cylindrical grains were present. The stress gradient in the central region was greater than that in the surrounding region. The stress was greater in the surrounding region because this region was squeezed by the mold. The maximum strain degree was 44.8% larger than the minimum strain degree. The local stress increment in each region was quantified. The stress increments of the three axes were in the range 14.2-19.5 MPa. This study examined the feasibility of evaluating the inner stress–strain state of PBX granules in a quantitative manner, which is significant in determining the inner strain and stress distribution in PBX granules during the molding process.

Keywords: technology of materials, testing and analysis, compression molding, polymer bonded explosive, state of stress, strain ellipsoid, X-ray tomography

1 Introduction

Development of polymer bonded explosives (PBXs) has attracted significant attention in recent years because they are emerging as important candidates in the field of high energy materials due to their lower susceptibility to shock and other stimuli. A PBX is obtained by mixing together a thermoplastic polymeric binder and explosive crystals to prepare the modelling granules, followed by compression molding. The density of a PBX is approximately proportional to its strength; however, whether the internal stress is distributed uniformly is closely related to a uniform distribution of density and *vice versa*. Consequently, a grain with good compactness and uniform density distribution has high strength, low stress, and excellent dimensional stability. For a PBX prepared by the compression molding process, the non-uniform distribution of internal stress during the compression process is the main factor leading to the non-uniform distribution of density. A comprehensive understanding of the development of stress induced by the compression molding process is critical in determining the properties of the granules. Moreover, a relatively high internal stress inside a PBX reduces the main mechanical properties, such as structural strength and fatigue life, leading to cracking and other phenomena for some time, thereby debonding the crystals from the binder and reducing the performance of the PBX. PBX molding granules, and the type of dispersed particle material, possess complex mechanical properties. According to the literature, the mechanical properties and movement of the aggregated explosive granules are different in pure solids or liquids, *i.e.*, stress is not uniformly distributed and the force is transmitted through the non-uniform force chain [1-4]. During compression molding, the stress testing method still lacks a relatively effective and accurate technique for measuring the internal structural strain of the granule material due to the presence of a significantly large amount of granules inside the PBX. Moreover, the test methods have been further found to be limited because of the complicated mode of action and distribution of the internal stress in a PBX during the compression process, as well as the explosive itself being a dangerous substance. Therefore, it is necessary to adopt a novel and effective method to measure the internal stress of a PBX, to investigate the stress distribution regularity of the PBX during compression, analyze the underlying generation mechanism of the stress distribution, and to improve the equilibrium distribution of the internal stress of the explosive.

Currently, the fundamental principle of a variety of internal stress testing methods is as follows: in the stress state some changes are induced that affect the material properties; therefore, the relationship between the effect and stress

is established. Finally, through measurements or calculations, the internal stress values and their distribution in the material can be obtained [5-18]. These methods mainly include destructive testing and non-destructive test. Destructive testing is more mature with higher precision. However, the use of destructive tests leads to a security risk because explosives are dangerous substances. Moreover, the cost and difficulties involved in the destructive methodologies for stress measurement have discouraged their use. Thus, the demand for a non-destructive test is becoming more crucial. For non-destructive testing, the most commonly used method is X-ray diffraction (XRD). However, the attenuation of X-rays is very rapid and can only penetrate the substance to a depth of a few microns. Therefore, the measurement by XRD only provides the stress for a nearly two-dimensional (2D) plane. Furthermore, a pre-fabricated strain gauge is used as a sensor to measure the internal stress, which is interfered with by the stress concentration at the edge of the explosive granules. Moreover, pre-fabricated strain gauges and other methods involve further deficiencies, such as difficulties in implantation, destruction of abrasive tools, and difficulty in measurement of the field distribution. Recently, some researchers have performed studies on the fracture mechanics of PBXs, micro strain measurement, and stress testing. Moreover, there is also little literature available on PBX micromechanics and strain measurement [9-11]. Yong *et al*. [12] tested residual stress of PBXs by an XRD method, and the results showed that residual stresses of the PBX were all draw stresses and the stress of the edge was larger than that of the central region. Dai *et al*. [13] investigated the micro–macro behaviour of 1,3,5-triamino-2,4,6-trinitrobenzene (TATB) granules by X-ray tomography and the discrete element model during the compacting process, and the results showed that the marginal region had the largest side pressure, finally forming a region with a large stress. Furthermore, real-time online monitoring technology has also been applied in some studies to investigate the mechanical properties of explosives and the distribution of the stress-strain field [19-20]. Zhou *et al*. [21] conducted real-time microscopic examination to observe the process of deformation and failure of PBX material by a semi-circular bend test using a scanning electron microscope equipped with a loading stage.

In the present study, TATB-based PBX granules were formulated using TATB powder and a fluoride binder by the aqueous suspension method. Spherical silicone rubber balls, prepared as strain markers, were implanted at different locations in the modelling granules to conduct simultaneously the compression experiment. Furthermore, the deformation characteristics of the silicone rubber balls after compression were observed by employing cone-beam computed tomography (CT) technology. According to the strain analysis of the strain markers in different

locations, by finite strain theory and strain ellipsoid, the local strain state in different locations was obtained, and the regional strain field was established to further predict the regional stress state. The internal stress distribution of the compressed grain was studied, which provided a research base for analyzing the microstructure and mechanical response during the compression process.

2 Finite Strain and Strain Ellipsoid

2.1 Finite strain

When an object is under an external force, progressive deformation, including incremental strain and finite strain, occur on the object under stress. The incremental strain, *i.e.*, instantaneous strain, is the infinitesimal strain at a moment during the deformation. The finite strain is the sum of the strain that has occurred at some stage during deformation, *i.e.*, it can be thought of as a sum of many infinitesimal strains. It is the change in the initial state and the final state of deformation, also known as total strain or bulk strain. The measurement of finite strain can provide an insight into the deformation and changes occurring in the regional strain state. The measurement principle and method are as follows: firstly, measurement of the morphological changes of the markers, with known original shapes, after deformation in a sample is carried out; based on an analysis of the strain markers (in this study the internally implanted standard silicone rubber balls were used as the markers), the finite strain ellipsoid is calculated. Through analysis and comparison, the linear strain and shear strain are calculated.

2.2 Strain ellipsoid

The basic view of a strain ellipsoid is based on the assumption that somewhere inside the object, before deformation, is a sphere. After deformation this sphere changes into an ellipsoid. This strain ellipsoid is the product of the deformation applied to a unit sphere. An ellipsoid with three principal strains, e_1, e_2, and e_3 as radii, is drawn. The ellipsoid represents the point of the entire strain state, and the ellipsoid is then designated as the strain ellipsoid. The corresponding equation is as follows:

$$\frac{X^2}{e_1^2}+\frac{Y^2}{e_2^2}+\frac{Z^2}{e_3^2}=1 \tag{1}$$

where: $e_1=\dfrac{L_1-L_0}{L_0}=\dfrac{\Delta L_1}{L_0}$, $e_2=\dfrac{L_2-L_0}{L_0}=\dfrac{\Delta L_2}{L_0}$, and $e_3=\dfrac{L_3-L_0}{L_0}=\dfrac{\Delta L_3}{L_0}$,

where L_1, L_2, and L_3 are the axial lengths after deformation and L_0 is the initial axial length.

Normally, the squared length ratio of the principal axis of strain before and after deformation, λ, is used as the three axes of the strain ellipsoid. In this case, the ellipsoid equation of the strain ellipsoid is represented as follows:

$$\frac{X^2}{\lambda_1}+\frac{Y^2}{\lambda_2}+\frac{Z^2}{\lambda_3}=1 \tag{2}$$

where:

$$\lambda_1=\left(\frac{L_1}{L_0}\right)^2=(1+e_1)^2,\quad \lambda_2=\left(\frac{L_2}{L_0}\right)^2=(1+e_2)^2,\text{ and }\quad \lambda_3=\left(\frac{L_3}{L_0}\right)^2=(1+e_3)^2,\ \lambda_1>\lambda_2>\lambda_3.$$

Analysis of the strain ellipsoid clearly indicates the geometric distribution of the internal stress state and the structure of an object when it is subjected to an external deforming force. The strain traces left by the deformed object could be obtained by non-destructive testing techniques, and a strain ellipsoid could be applied to obtain the status of the internal stress and its direction during deformation. The direction of the maximum deformed axis agrees well with the direction of the largest elongation (the minimum compression), and the direction of the minimum deformed axis is in good agreement with the direction of the smallest elongation (the maximum compression). Therefore, a strain ellipsoid can obviously reflect the nature of the stress in each direction at a point within the object.

3 Material Molding and Test Methods

3.1 Materials

The test materials employed in this study were TATB powder and fluoride binder (F2314) as granulated type and a TATB-based PBX was formulated by the aqueous suspension method. The sizes of the loosely packed granules were between 0.5 mm and 3 mm.

3.2 Compression molding test

3.2.1 Mold

Polyetheretherketone (PEEK), with a tensile strength of >200 MPa, was used as the compression mold. It can avoid metallic interference during the CT investigation. The size of the mold was Φ 20 × 40 mm^2, the aperture was 20 mm,

and the wall thickness was 5 mm. The height of the uncompacted specimen, after the granules had been added to the mold, was 40 mm.

3.2.2 Implantation of strain markers

Silicone rubber has good compressibility; therefore, it is easily deformed and it is easy to identify its shape features. Moreover, it also has excellent resistance to both low and high temperatures, being stable in the temperature range −60 °C to 250 °C. The compression of silicone rubber leads only to elastic deformation. The silicone rubber was made into 15 balls each with a diameter of 3.5 mm. The rubber spheres should not be too small because stress is a relatively macroscopic property and a continuous physical quantity. If the diameter of the rubber sphere were too small, its pressed deformation would be too random and disordered to form a strain ellipsoid. Therefore, in this case the deformation would have reflected the random micro-contact force between rubber spheres and the surrounding peripheral PBX particles, rather than the stress state of this region. However, rubber spheres with too large a diameter significantly affects the mechanical properties of the PBX. Below the diameter (3.5 mm) used in this study, the strains along the three principal axes of a rubber sphere could undergo significant changes, which facilitated image processing and size measurement, and simultaneously had no significant influence on the intrinsic compression property of the PBX.

The measured elastic modulus, E, obtained using a nano-indentation apparatus and a universal testing machine, of this silicone rubber at 80 °C was 2.14 MPa; and Poisson's ratio, ν, was 0.48. The 15 silicone rubber balls were implanted at different locations to investigate the strain state at different locations, as shown in Figure 1. All of the centres of the silicone rubber balls were at the medial surface of the mold, numbered in sequence as 1#-15#.

3.2.3 Compression molding

The compression test was performed by placing the mold in an INSTRON universal testing machine with an electronic temperature control box. The compression temperature was 80 °C, and the sample was compressed after holding it at the constant temperature for 20 min. The compression was divided into the following four stages: initially 5 MPa pressure was applied onto the mold, following which the pressure was maintained for 20 min before unloading. Subsequently, the sample was removed for CT scanning. Finally, the grains were re-pressed (3X), at compression pressures of 10 MPa, 20 MPa, and 30 MPa, respectively.

A simulated pressure preserving apparatus, as shown in Figure 2, was constructed. This figure clearly demonstrates that the upper pressure head moves downward under the action of the material testing machine and acts on

the particles, and when the pressure load achieves the assigned value, the upper pressure head stops. The objectives of adding constraint and preventing rebound can be achieved by immobilizing the position of the upper pressure head through adjusting nuts. The implanted rubber spheres exhibit a pure elastomeric state at the experimental temperature and only undergo elastic deformation. As long as the constraint of the upper pressure head is not removed, the rebound phenomenon of the rubber spheres would not occur.

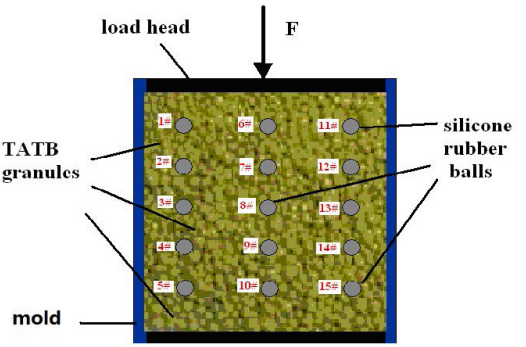

Figure 1. Locations of the implanted silicone rubber balls

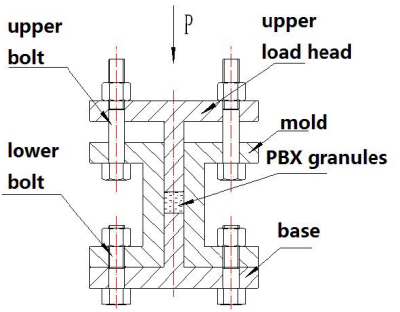

Figure 2. Simulated pressure preserving apparatus

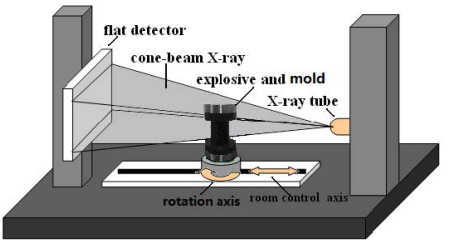

Figure 3. A schematic illustration of the CT scanning process

3.3 Cone-beam computed tomography test

The initial status was determined by cone-beam computed tomography (CT) scanning, and the CT test was repeated each time after pressure was applied. The voltage of the CT test was 130 kV, the current was 170 ìA, the magnifying factor was 18, and the minimum voxel size was 32 ìm. The mold was rotated through 360°, and a radial image based on X-ray absorption was obtained after each 0.3° rotation, as shown in Figure 3. To ensure consistency in changes in the granules and rubber slices, the CT test parameters were kept constant for each test.

4 Results and Discussion

4.1 Internal morphology of the sample and the deformation characteristics of the strain markers

Figure 4 demonstrates the axial CT results of grains under each compression pressure. Throughout the compression process, no obvious cleavage phenomena were observed for the molding powder granules; however, these powder granules underwent considerable plastic deformation. In the initial stages of compression, significant deformation of these granules occurred, and thus they became more compact. As the load was increased, many granules deformed into ellipsoids. Moreover, with the deformation of the granules and the rearrangement and rotation of some of the granules under force, the length-diameter direction of the modelling granules became arranged along the radial direction of the mold. An increase in temperature to 80 °C contributed significantly to the pore filling among the explosive granules, leading to easy aggregation of the granules. The binder was a thermo-sensitive polymer material, thus the increased temperature changed the mechanical properties of the binder and reduced its viscosity, thereby reducing the internal friction and decreasing the stress gradient. This facilitated the transmission of the compression pressure as well as an improvement in the uniformity of the stress distribution.

Figures 4 and 5 show the CT images of the longitudinal and cross sections of the explosive modelling granules and implanted strain markers (rubber balls), respectively, under different molding pressures. Figure 5 shows that during the entire compression process, the implanted rubber balls, in the cross section, are still of relatively regular circular-shape. However, the longitudinal sections in Figure 4 show that all of the rubber balls are deformed into oval shapes. Thus, it was preliminarily concluded that on the same plane, differences in the radial stresses of the grains was not significant. The grains had a larger strain in the axial direction, indicating the existence of larger axial stress.

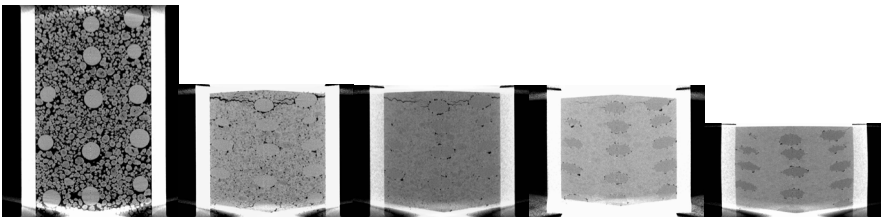

a. 0 MPa **b.** 5 MPa **c.** 10 MPa **d.** 20 MPa **e.** 30 MPa

Figure 4. CT images of the longitudinal sections of the grains under different compression pressures (medial surface)

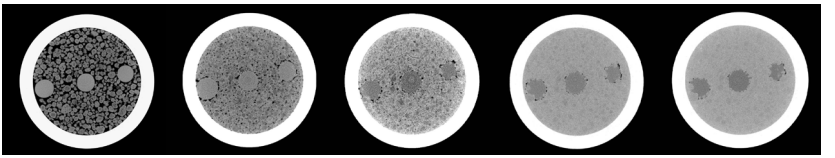

a. 0 MPa **b.** 5 MPa **c.** 10 MPa **d.** 20 MPa **e.** 30 MPa

Figure 5. CT images of the cross section of the PBX under different compression pressures

4.2 The influence of implanted strain markers on the compression properties of a PBX

The implanted rubber spheres might influence the compression properties of the PBX. In order to observe the influence of rubber spheres on the compression properties, related experiments were conducted in the absence of implanted rubber spheres and also by reducing the number of implanted rubber spheres. Figure 6 shows the CT images of samples without implanted rubber spheres and with five rubber spheres placed from top to bottom in the central region, under the same experimental conditions, before and after compression. Clearly, the PBX particles do not exhibit large deformation and the measurement results from every primary strain axis of the strain ellipsoid caused by five implanted rubber spheres are not very different from those caused by fifteen implanted rubber spheres.

Figure 7 shows the compressive stress-strain curves of samples without implanted rubber sphere, with five implanted rubber spheres, and with fifteen implanted rubber spheres, respectively. The figure clearly indicates that the stress-strain curves of the three cases basically follow identical trends. In the region with 0-60% strain, the stress-strain curves of the three samples exhibit a non-linear relationship. This is related to the existence of numerous pores at this stage, resulting in the occurrence of shear dislocation and rearrangement of

the PBX particles under the external load. Furthermore, when the strain reaches 60%, the particles are gradually compacted, resulting in an increase in density and strength, as well as compressive modulus.

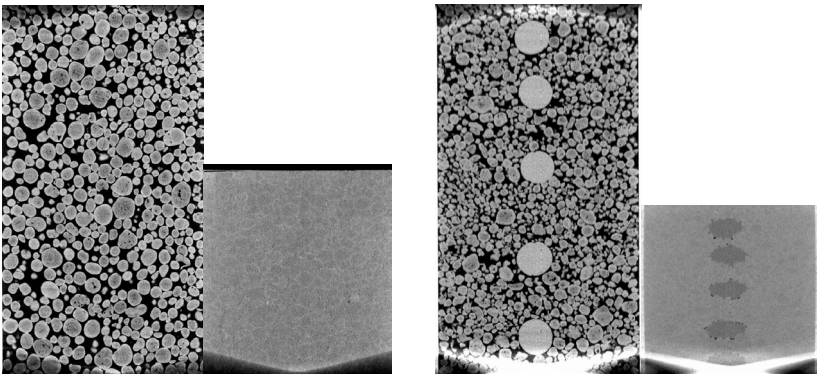

a. **b.**

Figure 6. CT images of samples without implanted rubber spheres (a) and with five implanted rubber spheres (b)

The presence of the implanted strain markers led to a slight increase in the volume compression of the PBX specimen compared to the ordinary PBX specimen. With the increase in the number of the strain markers, the elastic-plastic strain and the total strain of the PBX sample became larger. Under the same loading pressure, the PBX granule displacement, the porosity ratio, and the total strain, increased with an increasing number of the strain markers. When the number of strain markers was held constant, the particle displacement, density, and compressive modulus of the PBX increased with an increase in vertical pressure; at the same time, strain was greater than elastic strain. For PBX specimens containing strain markers, after a certain level of the effect of pressure on the particles to reduce the gap, further increases in the pressure resulted in compression deformation of the elastic rubber balls, thus leading to an increase in the total strain of the specimen. The main differences between the three samples occur in the stress range 0-20 MPa, due to the implanted strain indicators. Under the same strain conditions, the compressive stress of the samples with implanted strain indicators was found to be relatively small. However, for a compressive stress greater than 20 MPa, the stress-strain curves of the three samples are almost coincident, indicating that the influence of the strain markers on the compression properties of the samples themselves exists mainly in the initial stages of compression. When the samples are densely

compressed, the compressive moduli of the three samples are similar, indicating a weakening of the effect of the strain markers on the compression properties of the samples. The main objective of this study was only to obtain the distribution of internal stress and stress response status, rather than accurately calculating the stress value; therefore, no significant influence on the results was observed.

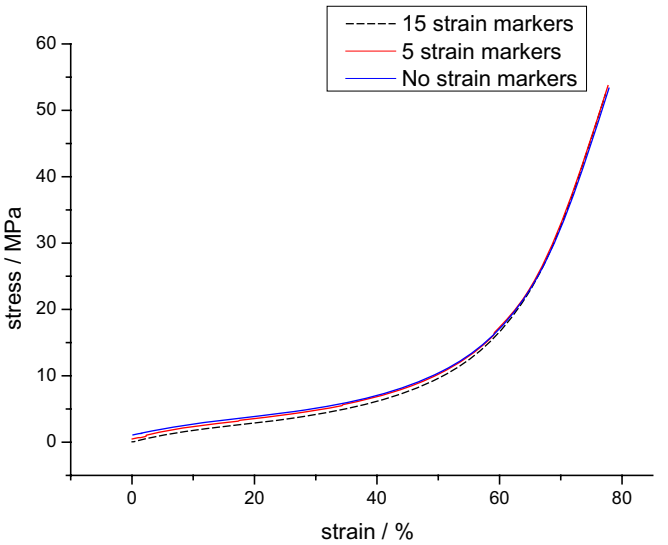

Figure 7. The compressive stress-strain curves of the three samples

4.3 Measurement of finite strain

Analysis of the finite strain can help to quantitatively evaluate the degree of change in the strain markers during deformation. Strain analysis is the premise of stress analysis. Inside the explosive, the implanted silicone rubber balls were initially spherical, which became distorted into an ellipsoid shape after deformation. After threshold segmentation of the CT image, the edge profiles of the 15 rubber balls inside the sample were extracted. The elongated direction of each rubber ball was selected as the X-axis; the section perpendicular to the X-axis was the YZ section; and the section perpendicular to the Y-axis was the XZ section. The lengths of the three axes of each rubber ball on the XY, XZ, and YZ sections were measured. The axial lengths after strain, L_x, L_y, and L_z, were obtained. The ellipsoid, with the lengths of L_x, L_y, and L_z as the lengths of the axes was the deformed ellipsoid, as shown in Figure 8. From the equation:

$$e_x = \frac{L_x - L_0}{L_0} = \frac{\Delta L_x}{L_0} \tag{3}$$

the elongations of each axis, *i.e.*, e_x, e_y, and e_z were calculated, where L_x, L_y, and L_z represent the axial lengths after deformation and L_0 is the initial axial length.

From the equation:

$$S_x = \frac{L_x}{L_0} = 1 + e_x \tag{4}$$

the length ratios of each axis, before and after deformation, S_x, S_y, and S_z, were calculated. If $S_x > S_y > S_z$, assuming $S_x = \mathrm{A}$, $S_y = \mathrm{B}$, and $S_z = \mathrm{C}$, then A, B, and C are the major axis, central axis, and minor axis of the deformed ellipsoid, respectively, *i.e.* A > B > C, as shown in Figure 9.

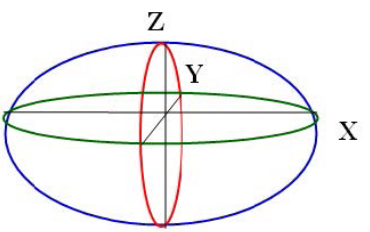

Figure 8. The schematic illustration of the deformed ellipsoid

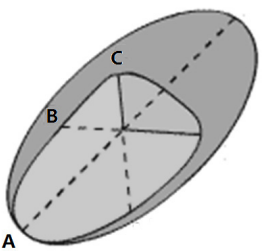

Figure 9. The schematic illustration of the strain ellipsoid

Then the principal strain ratios of the ellipsoid, $a = \mathrm{A/B}$ and $b = \mathrm{B/C}$, namely the axis ratios, were calculated. After obtaining the values of a and b, the Flinn parameter, $K = (\mathrm{a} - 1)/(\mathrm{b} - 1)$, and the strain degree, $r = a + b - 1$, of each rubber ball were obtained.

Table 1 lists the relative lengths, the axis ratios, the Flinn parameters, the

strain degrees, and the principal strain size ratios of the three principal strain axes of the 15 deformed ellipsoids under 30 MPa compression pressure.

Table 1. The analytical results of the measurement of finite strain

No.	Major axis [mm]	Central axis [mm]	Minor axis [mm]	Principal strain ratio, *a*	Principal strain ratio, *b*	Flinn parameter	Strain degree	Principal strain size ratio
	A	B	C	A/B	B/C	K	r	A:B:C
1	1.292	1.256	0.711	1.029	1.767	0.0374	1.795	1.817:1.767:1
2	1.326	1.21	0.669	1.096	1.809	0.1185	1.905	1.982:1.809:1
3	1.339	1.297	0.638	1.032	2.033	0.0314	2.065	2.099:2.033:1
4	1.388	1.331	0.64	1.043	2.080	0.0397	2.123	2.169:2.080:1
5	1.3435	1.3397	0.5966	1.003	2.246	0.0023	2.248	2.252:2.246:1
6	1.1831	1.1755	0.7526	1.006	1.562	0.0115	1.568	1.572:1.562:1
7	1.2292	1.1623	0.6586	1.058	1.765	0.0753	1.822	1.866:1.765:1
8	1.3279	1.2685	0.6172	1.047	2.055	0.0444	2.102	2.151:2.055:1
9	1.3438	1.2913	0.5816	1.041	2.220	0.0333	2.261	2.311:2.220:1
10	1.3096	1.3073	0.576	1.002	2.270	0.0014	2.271	2.274:2.270:1
11	1.2922	1.235	0.7227	1.046	1.709	0.0653	1.755	1.788:1.709:1
12	1.3055	1.2815	0.6686	1.019	1.917	0.0204	1.935	1.953:1.917:1
13	1.2916	1.2857	0.6078	1.005	2.115	0.0041	2.120	2.125:2.115:1
14	1.3118	1.2937	0.584	1.014	2.215	0.0115	2.229	2.246:2.215:1
15	1.3111	1.2939	0.5749	1.013	2.251	0.0106	2.264	2.281:2.251:1

The CT image is a shade of gray image, and measurement of an object is mainly dependent on differences in the gray level. The gray level at the edges of the object does not change suddenly; therefore, fixing the location of an object's edge is crucial for ensuring the accuracy of the measurement. Firstly, a measurement method was proposed and implemented, which was based on Zernike moment sub-pixel edge detection and polynomial fitting. Secondly, a measurement algorithm based on the integral of the sub-pixel contour rotation was proposed and implemented.

The dimensions of a standard sample with a length of 5 mm were measured by the already mentioned CT size measurement method (the true value was known to be 5 mm). The measurements were repeated ten times. Based on the corresponding true error between the measured and the true values, the root mean square error and standard deviation were calculated to be $m = \pm 0.03527$ and $S = 0.030389$. When measuring the length of every axis of the rubber spheres, the true length was unknown. Therefore, based on the corresponding probable error between the measured value and the arithmetic mean value of the measured

values, the root mean square error and standard deviation were calculated to be m = ±0.004884 and S = 0.004634. The measured length data listed in the tables are revised values, based on the error analysis.

4.4 Analysis of finite strain

The results listed in Table 1 were plotted into a Flinn diagram, as shown in Figure 10. The diagram may be applied to analyze the morphotype of each strain ellipsoid. The diagram is a 2D graph obtained by using the principal strain ratios *a* and *b* as axes, and (1,1) as the origin. Any point on the diagram represents the morphology and strain intensity of the strain ellipsoid. The Flinn parameter, *K*, is a shape parameter. The corresponding *K* value for a specific point can characterize the state of the strain ellipsoid, and the distance from the point to the origin (1,1) can characterize the strain intensity of the strain ellipsoid.

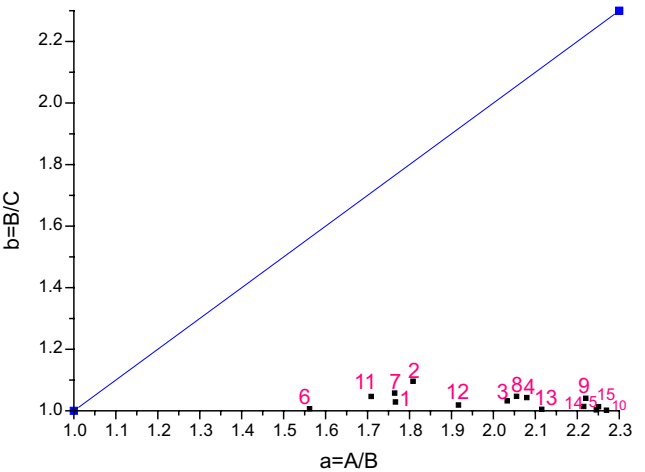

Figure 10. Flinn diagram obtained by strain analysis

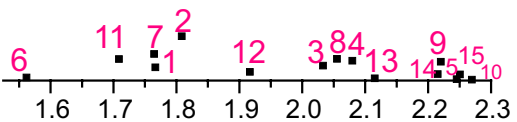

Figure 11. The regionally enlarged Flinn diagram

Based on the values of the Flinn parameter, *K*, the Flinn diagram was divided into several different deformation types: axisymmetric compression ($K = 0-0.15$); general compression ($K = 0.15-0.67$); plane strain ($K = 0.67-1.5$); general tensile ($K = 1.5-6.67$); and axisymmetric tensile ($K = 6.67-\infty$). A regional enlargement

of the Flinn diagram is shown in Figure 11. The average Flinn parameter of the 15 rubber balls was found to be $K = 0.034$, with a deviation between 0.0014-0.119. Thus, it seemed to be an axisymmetric compression, and the strain ellipsoid formed was a flat ellipsoid with compression mainly along one axis. The largest compression was in the C-axis direction, and the elongations in the A-axis and B-axis directions were similar. The principal strain size ratio also reflected similar results.

The three balls, 5#, 10#, and 15#, were all located at the bottom of the mold. Their corresponding points on the Flinn diagram were farthest from the origin and their strain intensity was the largest. However, the three balls, 1#, 6#, and 11#, were located at the top part of the mold, and their corresponding points on the Flinn diagram were nearest to the origin, indicating that the strain degree at the bottom was larger than that at the top. Ball 10# underwent the maximum strain, and its strain degree was 44.8% larger than that of ball 6# with the minimal strain.

Table 2. Statistics for each strain ellipsoid

Rubber ball No.	Length of X-axis [mm]	Length of Y-axis [mm]	Length of Z-axis [mm]	Elongation of X-axis	Elongation of Y-axis	Elongation of Z-axis	Rotation angle of X-axis relative to the horizontal line	Shear strain
	L_x	L_y	L_z	e_x	e_y	e_z	ψ	γ = tgψ
1	4.5233	4.3957	2.4884	0.2924	0.2559	−0.289	−14.48	−0.2582
2	4.2358	4.6395	2.3403	0.2102	0.3256	−0.3313	−32.16	−0.6288
3	4.6875	4.5411	2.2342	0.3393	0.2975	−0.3617	−24.74	−0.4608
4	4.6597	4.8577	2.2384	0.3313	0.3879	−0.3604	−19.78	−0.3596
5	4.7023	4.6889	2.088	0.3435	0.3397	−0.4034	−34.23	−0.6804
6	4.1409	4.1141	2.6342	0.1831	0.1755	−0.2474	1.34	0.0234
7	4.0682	4.3023	2.3051	0.1623	0.2292	−0.3414	3.54	0.0619
8	4.4398	4.6475	2.1603	0.2685	0.3279	−0.3828	1.6	0.0279
9	4.5194	4.7033	2.0356	0.2913	0.3438	−0.4184	0.84	0.0147
10	4.5835	4.5755	2.016	0.3096	0.3073	−0.424	4.37	0.0764
11	4.5228	4.3224	2.5295	0.2922	0.235	−0.2773	9.78	0.1724
12	4.4854	4.5692	2.34	0.2815	0.3055	−0.3314	16.54	0.2970
13	4.5	4.5207	2.1274	0.2857	0.2916	−0.3922	18.43	0.3332
14	4.5912	4.5278	2.044	0.3118	0.2937	−0.416	26.57	0.5001
15	4.5287	4.5889	2.0123	0.2939	0.3111	−0.425	27.45	0.5195

Table 2 lists the axial lengths and elongations of the three axes, the rotation angle of the X-axis with respect to the horizontal line, and the shear strain of the 15 rubber balls inside the grain under 30 MPa compression pressure. Most of the implanted rubber balls exhibited maximum elongation along the Z-axis, indicating a larger axial strain. Compared to balls in the peripheral region of the grain, a large deflection of the X-axis was barely observed relative to the horizontal line for balls 6#-10# located in the centre of the grain. However, the rubber balls at the two sides underwent larger clockwise rotation and larger counter clockwise rotation, respectively. This revealed that the stress in the central region of the grain was mainly axial stress from top to bottom with lower shear stress. Nonetheless, the peripheral region of the grain suffered not only from axial stress, but also a larger shear stress. This shear stress might have originated from the difference in size and direction of the friction between the mold and the explosive granules and the friction from the granules inside the grain.

4.5 Analysis of the stress field

From the data listed in Table 2, the corresponding deformed ellipsoid for each rubber ball inside the grain under 30 MPa could be drawn. As shown in Figure 12, the principal strain direction in each rubber ball in the X and Z directions is marked by arrows, corresponding to the main stress in the X and Z directions.

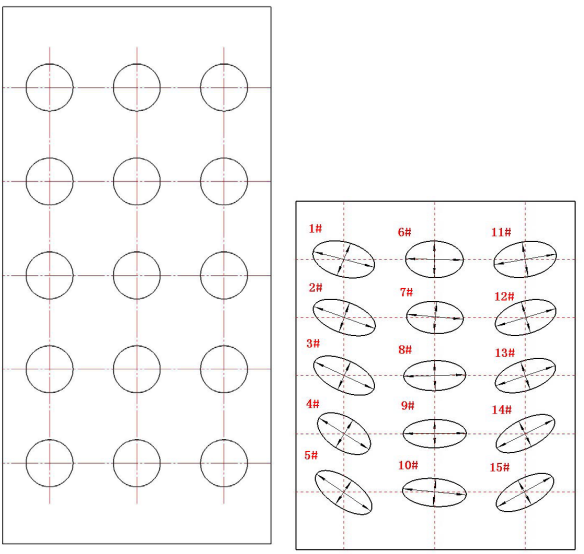

Figure 12. The stress field distribution and the deformed ellipsoids at 30 MPa

Hooke's law states that in an isotropic elastic object, the stress is proportional to the strain. Silicone rubber balls are elastic objects; therefore, based on the flexible linear strain on the principal strain axis and the constitutive relation of the silicone rubber material, the local stress can be calculated. According to the general Hooke's law, the stress increment on each principal stress axis can be obtained as follows:

$$\begin{cases} d\varepsilon_x = \left[d\sigma_x - \nu\left(d\sigma_y + d\sigma_z\right)\right]/E \\ d\varepsilon_y = \left[d\sigma_y - \nu\left(d\sigma_z + d\sigma_x\right)\right]/E \\ d\varepsilon_z = \left[d\sigma_z - \nu\left(d\sigma_x + d\sigma_y\right)\right]/E \end{cases} \tag{5}$$

where the elastic modulus E = 2.14 MPa and Poisson's ratio í = 0.48.

Table 3. Statistics of the increments of the three principal stress axes corresponding to each deformed ellipsoid

Rubber ball No.	$d\sigma_x$ [MPa]	$d\sigma_y$ [MPa]	$d\sigma_z$ [MPa]
1	14.9511	14.8983	14.9462
2	15.3493	15.5162	15.5244
3	17.8159	17.7555	17.8483
4	19.2116	19.2934	19.2536
5	19.3507	19.3452	19.4373
6	10.7797	10.7687	10.8726
7	12.9515	13.0482	13.2105
8	17.3787	17.4646	17.5440
9	18.7009	18.7768	18.8846
10	18.5087	18.5054	18.6741
11	14.3817	14.2990	14.3601
12	16.3425	16.3772	16.4147
13	17.2352	17.2438	17.3892
14	18.1753	18.1491	18.3259
15	18.2969	18.3217	18.4864

According to the data listed in Table 3, it may be concluded that the stress increments in the bottom region were relatively large. For example, the stress increments of the three axes at the location of ball 5# were 29.4%, 29.8%, and 30%, respectively, which were larger than those at the location of ball 1#. The stress increments of the three axes at the location of ball 10# were 71.7%, 71.8%,

and 71.8%, respectively, larger than those at the location of ball 6#. The stress increments of the three axes at the location of ball 15# were 27.2%, 28.1%, and 28.7%, respectively, were larger than those at the location of ball 11#. All these results indicate that the gradient increment of the internal stress from top to bottom of the central region is higher than that of the peripheral region, as shown in Figure 13. This might be related to the increased internal stress in the peripheral region squeezed by the mold. The results are similar to those of previous literature studies [12, 13].

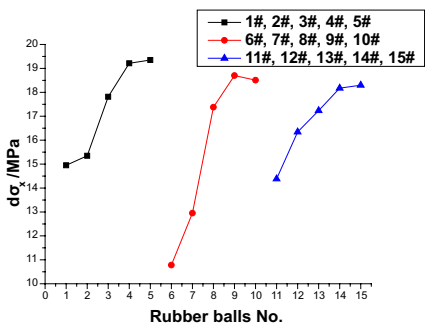

a. The stress increments of the X axis

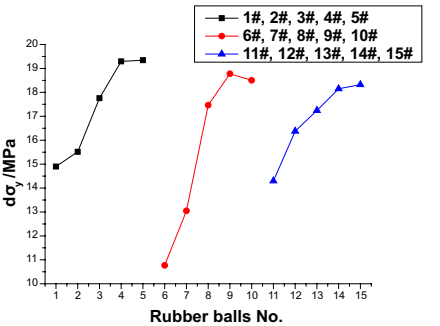

b. The stress increments of the Y axis

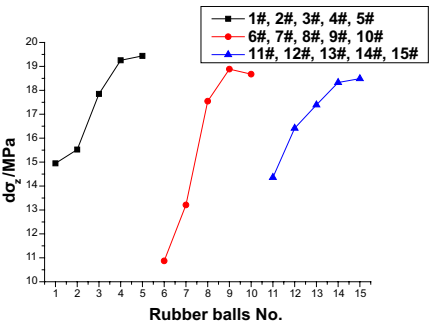

c. The stress increments of the Z axis

Figure 13. The stress increments of the three axes at the locations of balls 1#-15#

5 Conclusions

In this study, compression experiments were performed on TATB-based granules. Spherical silicone rubber balls were implanted into mold compacted TATB-based granules, and the deformation characteristics and regularity of the

strain markers after compression molding were observed by CT technology. Thus, strain analysis for the strain markers at different locations was carried out to obtain local strain states at different locations. The regional strain field was established, and furthermore the regional stress states were inferred. The conclusions were as follows:

(1) The internal strain was quantified. The maximum strain was 44.8% larger than the minimum strain.
(2) The local stress increment in each region was quantified. The stress increments of the three axes were in the range of 14.2-19.5 MPa.
(3) When the PBX was molded by compaction, each strain marker suffered from axisymmetric compression. The strain ellipsoid formed was flat ellipsoidal, with compression mainly along one axis.
(4) The stress in the central region of the grain was mainly axial stress from top to bottom, with slight shear stress; however, the peripheral region of the grain suffered not only from axial stress, but also larger shear stress.
(5) The gradient increment in the internal stress from top to bottom of the central region was higher than that in the peripheral region. This might be related to increased internal stress in the peripheral region squeezed by the mold.

References

[1] Hu, L.; Yang, P.; Xu, T.; Jiang, Y.; Xu, H. J.; Long, W.; Yang, C. S.; Zhang, T.; Lu, K. Q. The Static Friction Force on a Rod Immersed in Granular Matter. *Acta Physica Sinica* **2003**, *52*(4): 4.
[2] Chi, M. J.; Zhao, C. G.; Li, X. J. Stress-dilation Mechanism of Sands. *China Civil Engineering Journal* **2009**, *42*(3): 99-104.
[3] Geng, J. F.; Longhi, E.; Behringer, R. P.; Howell, D. W. Memory in Two-dimensional Heap Experiments. *Phys. Rev. E: Stat., Nonlinear, Soft Matter Phys.* **2001**, *64*(6): 30-60.
[4] Sun, Q. C.; Wang, G. Q. Force Distribution in Static Granular Matter in Two Dimensions. *Acta Physica Sinica* **2008**, *57*(8): 4667-4674.
[5] Xu, H.; Teng, H. C.; Cui, B.; Zhao, L. H.; Cao, Z. Y.; Jia, S. S. The State of the Art and Development on Nondestructive Residual Stress Measurement. *Phys. Test Chem. Anal.* (*Part A: Physical Testing)* **2003**, *39*(11): 595-598.
[6] Yong, Z. H.; Zhu, S. F.; Zhao, B. J.; Chen, J. H.; Zhang, W. B.; Wei, X. W. Residual Stress Test of Bonded Explosives by X-ray Diffraction Method. *Journal of Sichuan University (Engineering Science Edition)* **2007**, *39*(5): 101-105.
[7] Hao, R. J.; Tian, Z.; Chen, J. B.; Shen, C Y. Measuring Method of the Residual Stress of the Injection Plastic Parts. *Engineering Plastics Application* **2002**, *30*(5): 46-48.

[8] Zhou, H. P.; Li, J. M.; Li, L. Testing and Relieving of Residual Stress for Polymer Bonded Explosive Based on TATB. *Chin. J. Energ. Mater.* **2008**, *16*(1): 37-40.
[9] Baillou, F.; Dartyge, J. M.; Spyckerelle, C.; Mala, J. Influence of Crystal Defects on Sensitivity of Explosives. *Proc. 10th Symposium (Int.) on Detonation* **1993**, 816-823.
[10] Thompson, D. G.; Olinger, B.; DeLuca, R. The Effect of Pressing Parameters on the Mechanical Properties of Plastic Bonded Explosives. *Propellants Explos. Pyrotech.* **2005**, *30*(6): 391-396.
[11] Lewis, A.; Goldrein, T. Strain Measurement Techniques in Explosive. Discovery. *The Science & Technology Journal of AWE* **2004**, 36-43.
[12] Yong, Z. H.; Zhu, S. F.; Zhao, B. J.; Chen, J. H.; Zhang, W. B.; Wei, X. W. Residual Stress Test of Bonded Explosives by X-ray Diffraction Method. *Journal of Sichuan University (Engeering Science Edition)* **2007**, *39*(5): 101-105.
[13] Dai, B.; Zhang, W. B.; Lan, L. G.; Tian, Y. Experimental Study and DEM Simulation of Micro-Macro Behavior of TATB Granules During Compaction Using X-Ray Tomography. *Propellants Explos. Pyrotech*. **2015**, *40*(4): 688-698.
[14] Chen, J. H.; Zhao, B. J.; Zhu, S. F.; Yong, Z. H.; Zhang, W. B.; Wei, X. W. Study of Measuring Methods of Residual Stress in Polymer Bonded Explosives. *Journal of Sichuan University (Natural Science Edition)* **2005**, *42*(2): 296-299.
[15] Zhen, H. S.; Sun, Y. R.; Yuan, L. The Analysis and Prevention of Internal Stress in the Solid Rocket Motor Grain Flaw. *Aerospace Shanghai* **2002**, 5: 36-38.
[16] Wang, S. D. X-ray Method of Residual Stress Measurement in Explosive Charges. *Chinese Journal of Energetic Materials* **1994**, *2*(4): 35-39.
[17] Yong, Z. H.; Zhu, S. F.; Zhao, B. J. X-Ray Measurement of Residual Stress in Plastic Bonded Explosives. *J. Rare Earths* **2006**, *24*(2): 179-181.
[18] Zhang, W. B.; Zhao, B. J.; Tian, Y.; Huang, H.; Zhu, S. F.; Yang, Z. F. Ultrasonic Testing Stress of Polymer Bonded Explosive Specimens. *Chin. J. Energ. Mater.* **2006**, *14*(2): 136-138.
[19] Tan, W. J.; Li, M.; Tang, X.; Huang, H. Acoustic Emission in Compression of RDX Crystalline Particles. *Chinese Journal of Explosives & Propellants* **2009**, *32*(1): 21-24.
[20] Rae, P. J.; Palmer, S. J. P.; Goldein, H. T.; Field, J. E.; Lewis, A. L. Quasi-static Studies of the Deformation and Failure of PBX 9501. *Proc. Royal Society A.* **2002**, *458*: 2227-2242.
[21] Zhou, Z. B.; Chen, P. W.; Huang, F. L. An Experimental Study on the Micro/Macro Fracture Behavior of PBX using Digital Speckle Correlation Method. *Chin. J. High Pressure Phys.* **2011**, *25*(1): 1-7.